Systematics of low-lying states of even-even nuclei in the neutron-deficient lead region from a beyond-mean-field calculation

J. M. Yao,[1,2] M. Bender,[3,4] and P.-H. Heenen[1]

[1]*Physique Nucléaire Théorique, Université Libre de Bruxelles, C.P. 229, B-1050 Bruxelles, Belgium*

[2]*School of Physical Science and Technology, Southwest University, Chongqing, 400715, China*

[3]*Université Bordeaux, Centre d'Etudes Nucléaires de Bordeaux Gradignan, UMR5797, F-33175 Gradignan, France*

[4]*CNRS/IN2P3, Centre d'Etudes Nucléaires de Bordeaux Gradignan, UMR5797, F-33175 Gradignan, France*

(Received 9 November 2012; published 25 March 2013)

Background: Nuclei located in the neutron-deficient Pb region have a complex structure, rapidly evolving as a function of neutron and proton numbers. The most famous example is ^{186}Pb where the three lowest levels are 0^+ states, the two excited 0^+ states being located at low excitation energy around 600 keV. Coexisting structures with different properties are found in the neighboring nuclei. Many experiments have been performed over the last few years in which in-band and out-of-band γ-ray transition probabilities have been measured.

Purpose: A detailed interpretation of experimental data requires the use of a method going beyond a mean-field approach that permits to determine spectra and transition probabilities. Such methods have already been applied to selected isotopes in this mass region. Our aim is to provide a systematic investigation of this mass region in order to determine how well experimental data can be understood using a state-of-the-art method for nuclear structure.

Method: The starting point of our method is a set of mean-field wave functions generated with a constraint on the axial quadrupole moment and using a Skyrme energy density functional. Correlations beyond the mean field are introduced by projecting mean-field wave functions on angular-momentum and particle number and by mixing the symmetry-restored wave functions as a function of the axial quadrupole moment.

Results: A detailed comparison with the available data is performed for energies, charge radii, spectroscopic quadrupole moments, and $E0$ and $E2$ transition probabilities for the isotopic chains of neutron deficient Hg, Pb, Po, and Rn. The connection between our results and the underlying mean field is also analyzed.

Conclusions: Qualitative agreement with the data is obtained although our results indicate that the actual energy density functionals have to be improved further to achieve a quantitative agreement.

DOI: 10.1103/PhysRevC.87.034322 PACS number(s): 21.10.Re, 21.10.Ky, 21.60.Jz, 27.70.+q

I. INTRODUCTION

The study of the low-energy spectrum of neutron-deficient nuclei around ^{186}Pb has unveiled a rich variety of collective levels. In particular, several 0^+ states coexist at low excitation energy, which are in several cases the band head of a rotational sequence. This experimental result is interpreted as a manifestation of "shape coexistence"; i.e., a condition where states at similar excitation energy have distinctly different intrinsic shapes [1–5]. Many data support this interpretation. Direct evidence is, indeed, provided by the systematics of α-decay fine structure [4,6,7], by the moments of inertia of the rotational bands built on several 0^+ states [4], by in-band and intraband transition probabilities [8], by g-factor measurements [9,10], and by charge radii [11,12].

Let us first recall how the low-energy spectrum of the Pb isotopes around $N = 104$ is interpreted in terms of deformation. For all isotopes, much experimental evidence indicates that the ground states are predominantly spherical [5]. The two lowest excited 0^+ states have been associated with two deformed structures: an oblate one lower in energy in the isotopes above ^{188}Pb and a prolate one that is lower in lighter Pb nuclei. The crossing of these two structures in the excitation spectrum leads to the unique situation where the three lowest levels in ^{186}Pb are 0^+ states [7].

By contrast, the ground states of the Hg isotopes down to ^{180}Hg are interpreted as being oblate and weakly deformed with $\beta \approx -0.15$ [13,14]. From ^{198}Hg down to ^{190}Hg, the yrast states for a given angular momentum have almost constant excitation energies and are interpreted as the members of a rotational band based on the oblate ground state [15]. This simple pattern is distorted for the lighter even isotopes through the intrusion of a strongly deformed prolate band with $\beta \approx 0.25$ [3,4]. The excitation energies of the states in the prolate band evolve in a nearly parabolic manner as a function of the neutron number, cf., for example, Fig. 1 in Ref. [16] or Fig. 10 in Ref. [5].

The production rates of light Po isotopes are much smaller than those of the corresponding Hg and Pb isotones; hence, less experimental data have been collected, but they give a clear indication for an even more complex evolution of their structure as a function of neutron number. The heavier Po isotopes down to ^{196}Po have near-spherical ground states [5]. For $^{188–192}$Po, the analysis of their α-decay fine structure indicates that the ground-state wave function contains a significant contribution from deformed configurations [17]. Similar conclusions have been drawn from charge radii that indicate an increasing softness of the nucleus against quadrupole deformations with decreasing neutron number [18].

Our study will be limited to even-even nuclei. Let us, however, mention that data for odd-mass nuclei, where the low-lying spectrum can often be interpreted by the coupling of one particle to the low-lying states of the adjacent even-even nucleus, corroborate the interpretation of the spectral data

obtained for the light even-even isotopes of Hg, Pb, Po, and Rn [5].

There are two different approaches to interpret the complex and rapidly changing structure of nuclei in this mass region. One is based on the shell model, where the emergence of low-energy intruder states is interpreted as resulting from proton excitations across the $Z = 82$ closed shell [3,19,20]. Although the shell model including np-mh excitations across the shell gaps provides a consistent and microscopic description of the phenomenon of shape coexistence throughout the nuclear chart [5], the high dimensionality of the corresponding model space renders calculations for heavy open-shell nuclei untractable. For such nuclei, however, the np-mh excitations can be handled within the algebraic framework of the interacting-boson model, which truncates the shell-model space through the approximation of $J = 0$ and $J = 2$ coupled nucleon pairs treated as bosons [21,22].

An alternative and intuitive approach is based on mean-field methods, which provide a description of these structures in terms of shapes and deformed shells. In this framework, the low-lying spectrum is explained by the presence of multiple local minima in the deformation-energy surface. These minima can in turn be related to gaps in the single-particle spectrum. Although shape coexistence can be interpreted within pure mean-field models, a detailed description of the spectrum requires "going beyond the mean field" by means of symmetry restoration and taking into account fluctuations in the deformation degrees of freedom. The beyond-self-consistent mean-field method that has been developed by several groups combines the projection techniques with the generator coordinate method (GCM) [23–29].

Throughout this work, we use the axial quadrupole moment as a collective variable. Mean-field wave functions are constructed by Hartree-Fock (HF) + BCS calculations. They are projected on angular-momentum and particle number to form a basis of states that are mixed by the GCM. The interaction used here is the SLy6 parametrization of the Skyrme interaction that describes well the systematics of low-lying states of neutron-deficient Pb isotopes [30,31]. Selected results for some of the nuclei discussed here have already been published earlier [14,18,32–34].

The paper is organized as follows: In Sec. II, we give a brief outline of the method used to calculate the spectroscopic properties of low-lying states. In Sec. III, the calculated deformation energy curves, low-energy excitation spectra, charge radii, kinetic moments of inertia, and electric monopole and quadrupole transition strengths are presented and discussed in comparison with results of our previous study of Pb isotopes and the available data. A summary of our findings and conclusions is given in Sec. IV.

II. THE METHOD

As in our previous works [31], the starting point of our method is a set of self-consistent mean-field wave functions $|q\rangle$ generated with a constraint on the axial mass quadrupole moment $q \equiv \langle q|2z^2 - x^2 - y^2|q\rangle$. Dynamic correlations associated with symmetry restorations and fluctuations in the shape degree of freedom are introduced by particle-number and angular-momentum projection in the framework of the GCM. Limiting ourselves to axially symmetric configurations, the final wave function for the correlated state $|JM;k\rangle$ is given by the superposition of symmetry-restored mean-field wave functions

$$|JM;k\rangle = \sum_q f_k^J(q)|JMq\rangle, \tag{1}$$

where $k = 1, 2, \ldots$ labels different collective states for a given angular momentum J. The variable q is the generic notation for the deformation parameters. The symmetry-restored mean-field wave function is constructed as

$$|JMq\rangle = \frac{1}{\mathcal{N}_{J,M,q}} \sum_K g_K^J \hat{P}_{MK}^J \hat{P}^Z \hat{P}^N |q\rangle, \tag{2}$$

where $\mathcal{N}_{J,M,q}$ is a normalization factor. $\hat{P}_{MK}^J$ projects out eigenstates of $\hat{J}^2$ and $\hat{J}_z$ with eigenvalues $\hbar^2 J(J+1)$ and $\hbar M$ in the laboratory frame or $\hbar K$ in the intrinsic frame, respectively, whereas $\hat{P}^N$ and $\hat{P}^Z$ project out eigenstates of the particle-number operator for neutrons and protons with eigenvalues N_τ, $\tau = n, p$.

The weight functions $f_k^J(q)$ and the energies E_k^J of the states $|JM;k\rangle$ are the solutions of the Hill-Wheeler-Griffin (HWG) equation [35]

$$\sum_{q'} \left[\mathcal{H}^J(q,q') - E_k^J \mathcal{N}^J(q,q')\right] f_k^J(q') = 0. \tag{3}$$

The ingredients of Eq. (3) are the norm kernel $\mathcal{N}^J(q,q') = \langle JMq|JMq'\rangle$ and the energy kernel $\mathcal{H}^J(q,q')$, which in our calculation is given by a multireference energy density functional that depends on the mixed density matrix [36]. The formulas used to evaluate the energy and the norm kernels have been presented in Ref. [24].

The weight functions $f_\mu^J(q)$ in Eq. (1) are not orthogonal. A set of orthonormal collective wave functions $g_k^J(q)$ can be constructed as [37,38]

$$g_{Jk}(q) = \sum_{q'} (\mathcal{N}^J)^{1/2}(q,q') f_k^J(q'). \tag{4}$$

It has to be stressed, however, that the $|g_{Jk}(q)|^2$ quantity does not represent the probability to find the deformation q in the GCM state $|JM;k\rangle$. In addition, in the absence of a metric in the definition of the correlated state $|JM;k\rangle$, Eq. (1), the values of $g_{Jk}(q)$ for a converged GCM solution still depend on the discretization chosen for the collective variable q, which is not the case for observables such as the energies or transition probabilities.

Since the correlated states $|JM;k\rangle$ have good angular momentum, their spectroscopic quadrupole moments

$$Q_s(J_k) = \sqrt{\frac{16\pi}{5}} \begin{pmatrix} J & 2 & J \\ J & 0 & -J \end{pmatrix} \times \sum_{q',q} f_k^{J*}(q') \langle Jq'||\hat{Q}_2||Jq\rangle f_k^J(q) \tag{5}$$

and the reduced electric quadrupole ($E2$) transition strengths between them,

$$B(E2; J_i, k_i \rightarrow J_f, k_f) = \frac{1}{2J_i+1}\left|\sum_{q',q} f_{k_f}^{J_f *}(q')\langle J_f q'||\hat{Q}_2||J_i q\rangle f_{k_i}^{J_i}(q)\right|^2, \quad (6)$$

are calculated directly in the laboratory frame without approximation. The reduced matrix elements entering both expressions are determined as

$$\langle J_f q'||\hat{Q}_2||J_i q\rangle = \frac{(2J_f+1)(2J_i+1)}{2\mathcal{N}_{J_f,q'}\mathcal{N}_{J_i,q}}\sum_{M=-2}^{+2}\begin{pmatrix} J_f & 2 & J_i \\ 0 & M & -M\end{pmatrix} \times \int_0^\pi d\theta \sin(\theta) d^{J_i *}_{-M0}(\theta)\langle q'|e^{-i\theta \hat{J}_y}\hat{Q}_{2M}\hat{P}^N\hat{P}^Z|q\rangle, \quad (7)$$

where $\hat{Q}_{2M} \equiv er^2 Y_{2M}$ is the electric quadrupole moment operator. To relate the moments in the laboratory frame to intrinsic deformation parameters, one can define two dimensionless quadrupole deformations in the same way as in the static rotor model. The first one, $\beta^{(s)}$, is related to the spectroscopic quadrupole moment (for states in a $K = 0$ band) by

$$\beta^{(s)}(J_k) = \sqrt{\frac{5}{16\pi}}\frac{4\pi}{3ZR^2}\left(-\frac{2J+3}{J}\right)Q_s(J_k), \quad (8)$$

and the second, $\beta^{(t)}$, is related to the reduced $E2$ transition strength:

$$\beta^{(t)}(J_i, k_i \rightarrow J_f, k_f) = \frac{4\pi}{3ZR^2}\sqrt{\frac{B(E2; J_i, k_i \rightarrow J_f, k_f)}{e^2\langle J_i 020|J_f 0\rangle^2}}. \quad (9)$$

The radius R appearing in both expressions is given by $R = 1.2A^{1/3}$ fm, with A being the mass number and $\langle J_i 020|J_f 0\rangle$ is a Clebsch-Gordan coefficient. The nuclear matrix element entering the electric monopole decay from $|JM;k\rangle$ to $|JM;k'\rangle$ through the emission of conversion electrons is determined by

$$\rho^2_{E0}(J_k \rightarrow J_{k'}) = \left|\frac{\langle JM;k'|e\sum_p r_p^2|JM;k\rangle}{eR^2}\right|^2, \quad (10)$$

where p is an index running over all proton single-particle states. Since the electric transition matrix elements are calculated in the full model space of occupied single-particle states, there is no need to introduce effective charges, and we use the bare charge for protons instead.

As in our previous works [31], pairing correlations are treated to the BCS approximation, including the Lipkin-Nogami (LN) prescription to avoid a collapse of pairing correlations when the density of single-particle levels is too low. The mean-field wave functions are discretized on a three-dimensional cartesian mesh, with a distance between mesh points of 0.8 fm sufficient to have an accuracy much better than 100 keV on energy curves. The number of points considered in the solution of the HWG equation is also large enough (up to 50 points in the most complicated topographies) not to affect any of our conclusions on spectra and transition probabilities. The parametrization SLy6 [39] of the Skyrme interaction and a density-dependent zero-range pairing force with the same strength of -1250 MeV fm^3 for neutrons and protons and a soft cutoff at 5 MeV above and below the Fermi energy as defined in Ref. [40], are adopted in the construction of mean-field wave functions and the configuration mixing calculations. As required by the SLy6 parametrization, the full two-body center-of-mass correction is included in the variational equations to generate the mean field and in the calculation of the projected GCM energies.

III. RESULTS AND DISCUSSION

A. General comments

In mean-field models, self-consistent and non-self-consistent ones alike, there is an intimate relation between the total binding energy and the density of levels around the Fermi energy in the Nilsson diagram of single-particle energies. This is obvious for non-self-consistent macroscopic-microscopic models, where the extra binding from shell structure is explicitly calculated as a "shell correction" to the total binding energy, and, therefore, can be easily isolated, but the same mechanism is hidden in the total energy of self-consistent mean-field models. A lower-than-average density of single-particle levels around the Fermi energy results in extra binding, whereas a larger-than-average value reduces binding. Therefore, large gaps near the Fermi energy in the Nilsson diagram often correspond to minima in the deformation energy curve, whereas a large bunching of levels close to the Fermi energy usually corresponds to barriers between such minima. The Fermi energy does not have to be located exactly at the gap, but might be slightly below or above it. With increasing distance of the Fermi energy from the gap, however, the shell effect can be expected to become less pronounced. In any event, shape coexistence is the fingerprint of a variation of shell structure around the Fermi energy that opens or closes gaps with deformation.

To have near-degenerate collective states with the same quantum numbers but different deformations, there has to be a mechanism that prevents their mixing. As states of different deformations are *a priori* not orthogonal, the diagonalization of the Hill-Wheeler-Griffin equation (3) can easily produce collective wave functions spread over a large range of deformations. Large nondiagonal energy kernels will amplify this effect. Therefore, the sole presence of a large barrier between the minima is not sufficient to prevent mixing. To achieve a weak coupling between mean-field configurations, the matrix elements of the overlap and the energy kernels between them must be small. A mechanism leading to such suppression of the matrix elements is provided by intruder states; i.e., single-particle levels that are downsloping with deformation from the next major shell and, therefore, have a parity opposite to that of the levels at the Fermi energy. Assuming conserved parity and neglecting pairing correlations, two HF states with a different number of positive-parity and negative-parity single-particle levels do not overlap and are weakly coupled in the GCM. This is no longer the case when pairing correlations

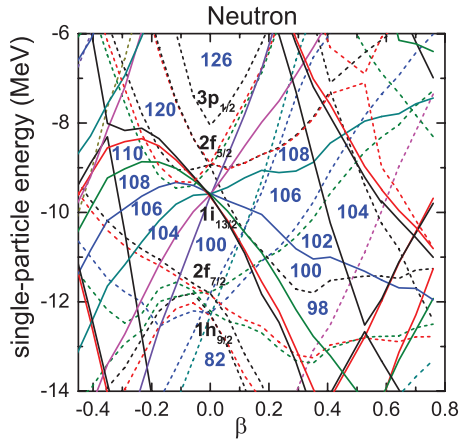

FIG. 1. (Color online) Nilsson diagram of the eigenvalues of the single-particle Hamiltonian for neutrons in ^{190}Po as a function of the axial deformation parameter β, obtained with the Skyrme interaction SLy6; see Eq. (11).

are taken into account, but one can expect that the overlap between the mean-field wave functions remains small.

The detailed results of this extensive study are available in the Supplemental Material [41]. They include excitation energies, charge radii, spectroscopic quadrupole moments, and electric monopole and quadrupole transition strengths for the low-lying states that were computed for total angular-momentum values up to $J = 10\hbar$, in the neutron-deficient $^{176–194}$Hg, $^{180–194}$Pb, $^{186–210}$Po, and $^{194–204}$Rn isotopes. We focus here on the evolution of low-lying states with neutron and proton number and discuss the similarities and differences between these four isotopic chains.

B. Nilsson diagrams

Figures 1 and 2 display the Nilsson diagram of neutron and proton single-particle energies as a function of a dimensionless quadrupole deformation parameter β. This parameter is related to the intrinsic mass quadrupole moment q of the HF + BCS states by the relation

$$\beta = \sqrt{\frac{5}{16\pi}}\frac{4\pi}{3AR^2}q. \tag{11}$$

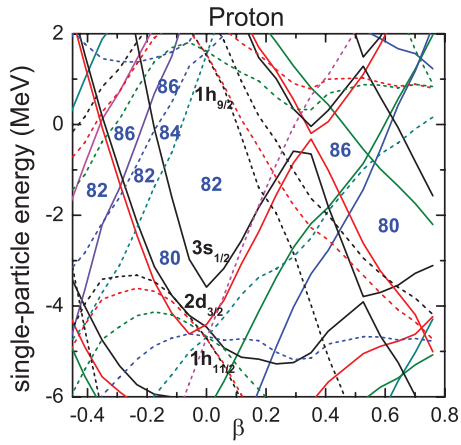

FIG. 2. (Color online) Same as Fig. 1, but for the protons.

There is a large number of gaps visible in the Nilsson diagram for neutrons. First, there is a spherical one at $N = 100$, below the $1i_{13/2^+}$ intruder level. There are many deformed gaps of slightly varying size on the oblate side for every even neutron number from $N = 102$ to $N = 110$ at increasingly large deformations up to $\beta \simeq -0.2$. These gaps are all located between the spreading magnetic substates of the $1i_{13/2^+}$ shell. There are also gaps of varying size for every even neutron number between $N = 98$ and $N = 108$ on the prolate side. Due to the downsloping $K = 1/2$ level from the $2g_{9/2^+}$ shell above and the upsloping levels from the $1h_{9/2^-}$ shell below, however, they correspond to configurations with a different number of occupied intruder levels. Because of several level crossings, the deformations of the gaps on the prolate side are not ordered according to N. The largest ones are $N = 106$ for $\beta \simeq 0.3$ and $N = 104$ for $\beta \simeq 0.5$, respectively.

For the protons, there is a large spherical shell gap at $Z = 82$, a gap at $Z = 80$ extending from sphericity to an oblate shape with β values down to -0.2 as well as a smaller oblate $Z = 82$ gap at $\beta \simeq -0.25$. At normal deformation, there are no significant proton gaps on the prolate side that come close to the Fermi energy, except for a small $Z = 86$ one at $\beta \simeq 0.5$.

At the deformation corresponding to the deformed neutron gaps, the downsloping high-j proton intruder orbitals have dropped to energies close to the Fermi energy, in most cases even well below, and thus have a sizable occupation. For this reason, some single-particle orbitals composing the corresponding deformed mean-field wave function are very different from those of the spherical configuration and the overlap between both is small. As discussed above, a small overlap creates favorable conditions for a decoupling between configurations corresponding to different shapes.

We have checked that the Nilsson diagrams of both protons and neutrons change only marginally for the nuclei covered in the present study.

C. Systematics of deformation energy curves

The energy curves obtained after projection onto particle numbers are presented in Fig. 3. The mean-field ground states for all neutron-deficient Pb isotopes are spherical. The same result has been obtained in calculations using the parametrization D1S of the Gogny force [42]. However, it can be modified by a lower pairing strength [43] or the use of a different pairing functional [44]. For all Pb isotopes except $^{180–182}$Pb, the curves also display an oblate minimum with $\beta \simeq -0.20$. The excitation energy of this minimum decreases from 0.76 to 0.50 MeV for N going from 112 to 108, and increases again up to 1.63 MeV when decreasing the neutron number further down to 102. The well depth follows a similar evolution. It starts from 0.46 MeV for $N = 112$, is maximal at 0.93 MeV for $N = 108$, and decreases again down to 0.49 MeV for $N = 102$. On the prolate side, the energy curves present an inflexion point at $\beta \simeq 0.30$ for $N \geqslant 110$ and a minimum for lower N values down to 100. The excitation energy of this minimum decreases from 1.47 MeV in ^{190}Pb down to 0.61 MeV in ^{184}Pb and rises up again to 0.82 MeV in ^{182}Pb.

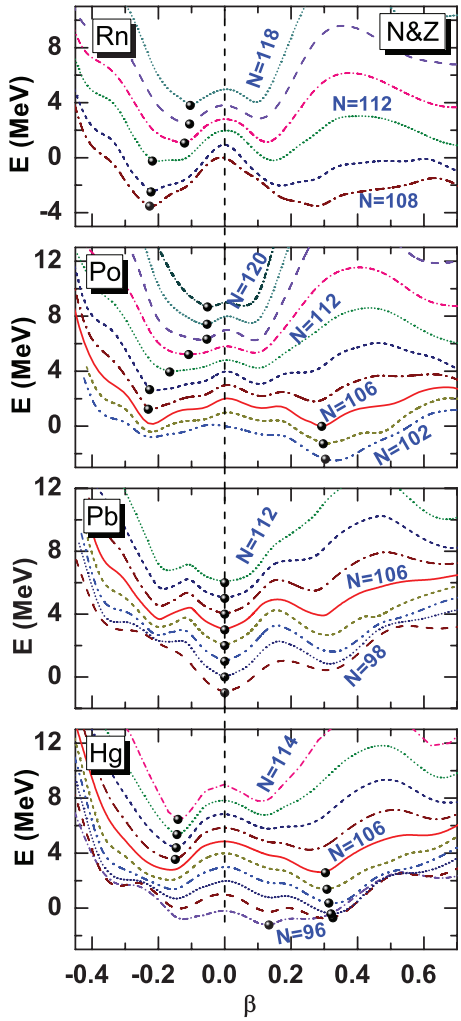

FIG. 3. (Color online) Energy curves for the particle-number-projected HF + BCS states ($N\&Z$) for $^{176-194}$Hg, $^{180-194}$Pb, $^{186-204}$Po, and $^{194-204}$Rn as a function of the intrinsic quadrupole deformation parameter β. All energies are normalized to the spherical shape ($\beta = 0$), but with an additional energy shift of 1 MeV between two neighboring isotopes. The lowest configuration of a given nucleus in the deformation region of interest is indicated with a bullet.

The deformation of the prolate minima of the Pb isotopes follows closely the neutron gaps in the Nilsson diagram. Their deformation is $\beta_2 \simeq 0.32$ for $N = 100$ increases slightly at $N = 102$, and then decreases up to $N = 106$. For $108 \leqslant N \leqslant 112$, this prolate minimum disappears as the Fermi energy approaches a region with densely bunched levels in the Nilsson diagram.

There are no spherical minima for the Hg, Po, and Rn isotopes discussed here. The minima of the deformation energy curves for these nuclei are not always in a one-to-one correspondence with the gaps in the Nilsson diagram. This is because the gap for one nucleon species is often located at a deformation corresponding to densely bunched levels for the other. Hence, the minima correspond to the most favorable compromise between the shell effects for neutrons and protons.

The ground states that we obtain for the Hg isotopes are oblate above $N = 106$ and prolate below this neutron number. At $N = 106$, the oblate and prolate minima are nearly degenerate. The energy curves are very shallow for $N = 98$ and 96. The deformation of the oblate minimum corresponds to the $Z = 80$ proton gap for all values of N, whereas the prolate minima of the isotopes with $N \geqslant 98$ correspond to the many gaps obtained in the neutron Nilsson diagram around $\beta \simeq 0.3$. For the soft $N = 96$ isotope, the prolate minimum is shifted to a weakly deformed configuration with $\beta \simeq 0.13$, close in energy with the weakly deformed oblate minimum. The oblate minimum is very rigid for $N = 114$ and becomes softer with decreasing N. Such a behavior can be related to the neutron single-particle levels close to the Fermi energy. For $N \geqslant 108$, the density of neutron levels is high and their energy is rapidly increasing when β becomes more negative. The situation changes at $N = 106$ and below, where the density of neutron levels is low and the energy varies more slowly with deformation.

The energy curves of the Po isotopes evolve in a way similar to those of the Hg isotopes. In particular, the transition between oblate and prolate ground states appears at the same neutron number. However, there are differences in the details. The oblate minimum is always shallower, and the oblate deformation of the ground state increases steadily with decreasing N. For $N = 108$, which corresponds to the lightest Po isotope with an oblate ground state, the deformation parameter β is significantly larger for Po than for Hg. By contrast, for $102 \leqslant N \leqslant 106$ the prolate ground states have a smaller deformation for Po than for the corresponding Hg isotopes.

The energy curves of the Rn isotopes evolve in a way similar to those of the Po isotopes, but with deeper oblate and prolate minima.

Our calculations are limited to axial deformations. One cannot exclude, however, that in some cases the minima appearing in the axial deformation energy curves actually correspond to saddle points of the energy surface in the full β-γ plane. Several scenarios are possible. First, the axial minima can be separated by a barrier with the energy rising all the way from both sides, such that they are true minima. In Ref. [31], we have checked that this is the case for the spherical, prolate, and oblate minima found in the $^{182-194}$Pb isotopes studied there. But there could be cases where there is no barrier between the axial minima. A second possibility is that the energy changes monotonically from $\gamma = 0^\circ$ to 60°. Then, the higher-lying minimum is in fact a saddle point. This happens for many well-deformed nuclei, and also for many γ-soft ones. A third case occurs when there is a triaxial minimum between the two axial ones. In this case, depending on the appearance of barriers, one or even both minima in the axial energy curve might be saddle points.

The Gogny interaction D1s very often gives deformation energy surfaces very similar to those obtained with the Skyrme interaction SLy6 used here. A systematic survey of energy surfaces in the β-γ plane using D1s can be found in Ref. [45]. For the nuclei studied here, the study of Ref. [45] indicates that minima found in a calculation restricted to axial shapes have to be suspected to be saddle points when the ground state and the secondary minimum in the axial energy curve are nearly degenerate and are obtained for similar values for $|\beta|$.

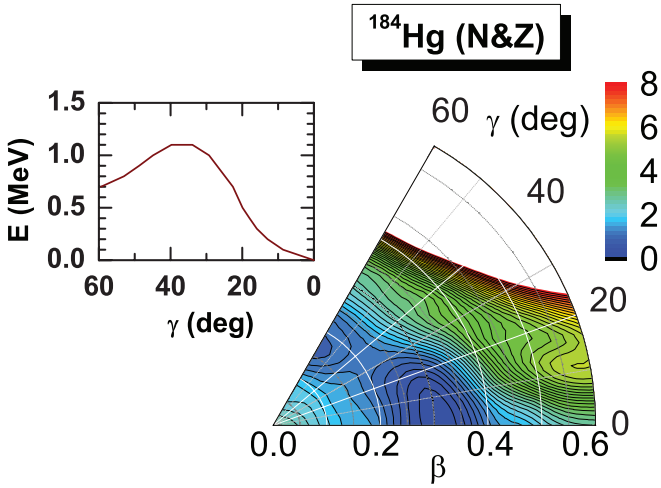

FIG. 4. (Color online) Quadrupole deformation energy surface for ^{184}Hg, normalized to the absolute minimum and projected on particle numbers. Each contour line is separated by 0.2 MeV. The inset shows the energy as a function of γ deformation along the path joining the two axial minima.

Two examples of particle-number projected energy surfaces in the full β-γ plane obtained with SLy6 are displayed in Fig. 4 for ^{184}Hg and Fig. 5 for ^{200}Po. The variation of the energy as a function of γ for a path going from the oblate to the prolate minimum is shown as an inset in the figures.

Figure 4 illustrates the case where there is small barrier between the two minima. For ^{200}Po, the absolute minimum is obtained for a nonaxial configuration, with $\beta \approx 0.1$ and $\gamma \approx 10^{\circ}$. This nucleus is a rare case where both minima found in an axial energy curve actually correspond to saddles in the full β-γ plane [46]. The prolate saddle is at almost the same $|\beta|$ value as the nearby triaxial minimum and is located just about 100 keV higher, whereas the oblate saddle is at somewhat smaller $|\beta|$ values and higher excitation energy. The heaviest Po and Rn studied here can be expected to have deformation energy surfaces of similar γ-soft topography, although not necessarily with a triaxial minimum.

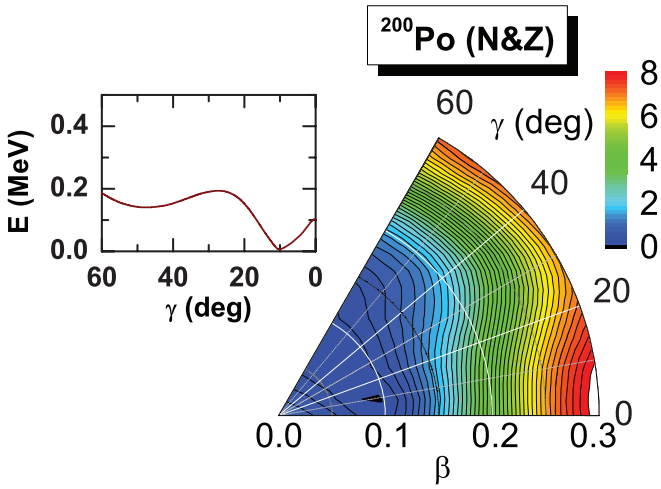

FIG. 5. (Color online) Same as Fig. 4 for ^{200}Po.

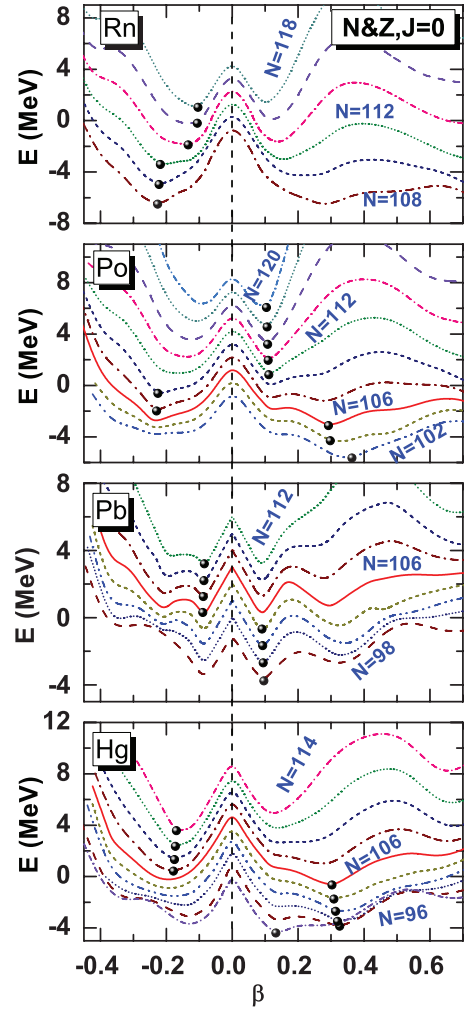

FIG. 6. (Color online) Same as Fig. 3, but with projections onto both particle numbers and angular momentum $J = 0$.

D. Effects of angular-momentum projection on energy curves

The energy curves projected on $J = 0$ are given in Fig. 6. The energies are drawn at the intrinsic quadrupole moment (or the β value) of the mean-field wave function that is projected. This is the most convenient way to plot the results obtained after projection on angular momentum. However, it has to be kept in mind that, after angular-momentum projection, it is only at large deformation and for $J > 0$ that the β value of Eq. (11) provides a rough estimate for the values obtained through Eqs. (8) or (9) from observable quadrupole moments. At small deformations, the intrinsic deformation does not have a relation to an observable. Therefore, the interpretation of these energy curves requires some caution [31,42]. The energy $\Delta E_{\rm rot} \equiv E_{J=0}(\beta) - E(\beta)$ gained from the restoration of rotational symmetry is displayed on the bottom panel of Fig. 7 for ^{186}Hg, ^{188}Pb, and ^{190}Po. The spherical configuration is purely a $J = 0$ configuration; hence, projection on $J = 0$ does not bring any gain of energy. A slight deformation of the mean-field is sufficient to introduce higher J components (or, in a shell-model language, particle-hole excitations) in the mean-field wave function. Projection on $J = 0$ gives then an energy gain, which at small deformation is almost symmetrical

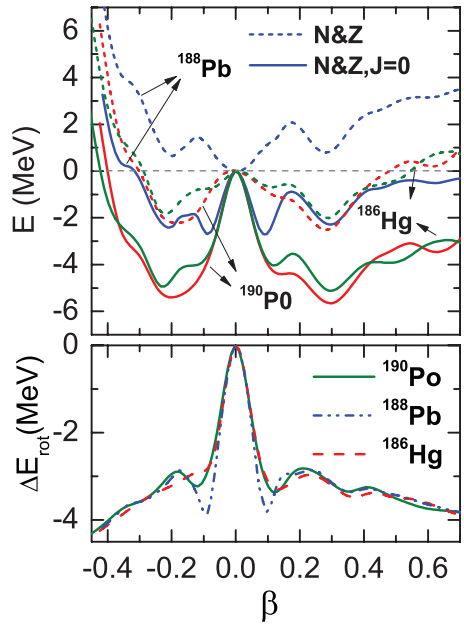

FIG. 7. (Color online) Effect of projection on $J = 0$ on topography of deformation energy curves at small deformation. Top panel shows energy curves after projection on particle numbers ($N\&Z$) and on angular momentum $J = 0$ as a function of β for ^{186}Hg, ^{188}Pb, and ^{190}Po. Lower panel shows the corresponding energy gained from projection on $J = 0$; $\Delta E_{\rm rot}(\beta) = E_{J=0}(\beta) - E(\beta)$.

around the spherical point and increases rapidly (in absolute value) to reach about 3 MeV around $|\beta| \approx 0.1$. At larger deformation, the energy gain still increases further, but at a slower rate, as illustrated in Fig. 7. For nuclei with deformed minima, this generic behavior usually makes the energy curve more rigid at small deformation values and softens it at larger ones. For nuclei with a spherical minimum in the mean-field energy surface, such as the Pb isotopes, the minimum is shifted to small absolute values of the deformation β for all values of γ, forming a kind of "Mexican hat" around the spherical point.

Neither the mean-field wave functions nor the wave functions obtained for a given set of quantum numbers after symmetry restoration are orthogonal. The overlap between $J = 0$ wave functions is large for all small deformation values of the mean field. It turns out that the states "at the bottom of the mexican hat" are not only almost degenerate, but also have very large overlaps close to one, meaning that after projection they describe the same physical state. We will call a state in this very particular minimum a "correlated spherical state". This state has the property to appear only for $J = 0$ values, but not for higher angular momenta; therefore, it is not the head of a rotational band. This allows us to distinguish the correlated spherical states from "truly deformed" minima at small deformation that appear at all J and lead to the appearance of a rotational band. In any event, at small deformation, the labeling of projected wave functions by a mean-field deformation has a very limited meaning.

The main findings for the effect of projection on $J = 0$ on the energy curves of the nuclei discussed here are

(i) Using the definition of a correlated spherical state, the ground state is spherical for all Pb isotopes. A prolate minimum around $\beta \simeq 0.3$ is obtained for the lightest isotopes up to $N = 106$. The oblate minimum that was obtained before projection on angular momentum for isotopes above $N = 106$ is not clearly visible anymore, as it merges with the spherical minimum.

(ii) For the Hg, Po, and Rn isotopes, angular-momentum projection does not modify the topography of the energy curves significantly. Both the prolate and the oblate minima become more bound with respect to the energy of the spherical point. For some nuclei, the minimum is also shifted to slightly larger deformation.

(iii) For Po isotopes with $112 \leqslant N \leqslant 120$, the absolute minimum of the energy curves moves from an oblate to a prolate shape after projection on $J = 0$. These Po nuclei are the only ones where projection results in a change of the sign of the deformation.

When triaxial shapes are included, angular-momentum projection shifts the deformed minima from axial shapes to slightly nonaxial ones [26–28], in the same manner as the spherical minimum is shifted to slightly deformed intrinsic shapes. For light nuclei, symmetry-restored GCM calculations including triaxial shapes have been performed and this shift does not qualitatively change the interpretation of the minima. Because of their high computational cost, such calculations have not been performed yet for nuclei as heavy as the ones discussed here within an energy-density-functional framework.

While the mean-field ground states are at normal deformation for all nuclei considered here, we have to note that after angular-momentum restoration, the ground states of ^{186,188}Po and ^{194,196}Rn correspond to the projection of a superdeformed configuration beyond the range of deformations displayed in Fig. 6. A similar result for the lightest Po and Rn isotopes is also obtained when using the Gogny D1s force and adding a rotational correction [45]. This finding is the consequence of the energy gain from angular-momentum projection growing with deformation, cf. Fig. 7. It is in contradiction with the data and is an artefact of the low surface-energy coefficient $a_{\rm surf} = 17.7$ MeV of the parametrization SLy6. We have checked that, with the SLy4 parametrization, which has a slightly larger surface-energy coefficient of $a_{\rm surf} = 18.4$ MeV, the deformation energy curves are stiffer such that the superdeformed minima remain above the normal deformed ones after projection. On the other hand, at the mean-field level, the relative excitation energies of the various minima in the Pb region are much better described by SLy6 because, overall, SLy4 gives excitation energies that are too large. A similar result has been found for ^{240}Pu in Ref. [29]. This points to the need to fit dedicated parametrizations for beyond-mean-field calculations in the future. We have limited our configuration mixing calculations to deformations up to $\beta \approx 0.6$. We have checked that the normal- and superdeformed states are sufficiently decoupled that the low-lying states at

normal deformation discussed here are not affected by using these restricted configurations.

E. Systematics of low-lying 0^+ states

1. Collective wave functions

The collective wave functions $g_k^J(q)$, as defined by Eq. (4), are spread over a large range of deformed mean-field wave functions. However, it is often still possible to classify them as spherical, oblate, or prolate by looking at the dominant configurations. Such a classification is greatly helped by studying the mean deformation of the mean-field components of a collective wave function defined by

$$\bar{\beta}_{Jk} \equiv \sum_q \beta(q)|g_{Jk}(q)|^2. \tag{12}$$

This quantity has to be taken with a grain of salt. First, because of the nonorthogonality of the basis of projected mean-field states, $|g_{Jk}(q)|^2$ does not represent the probability to find a given mean-field state $|q\rangle$ in the projected GCM state $|JM;k\rangle$. Second, $\bar{\beta}_{Jk}$ cannot be expected in general to correspond to a deformation deduced from electromagnetic transitions or spectroscopic moments. Still, this quantity turns out to be useful when analyzing the mixing of oblate, spherical, and prolate wave functions. For simplicity, we will label the collective states as oblate, prolate, or spherical when the mean deformation $\bar{\beta}_{Jk}$ has a value close to the deformation of the mean-field state with the largest weight in the collective wave function. When this is not the case, the state will be denoted as "spread".

The collective wave functions $g_{Jk}(q)$, Eq. (4), of the lowest $J = 0$ states are plotted in Figs. 8–11 as a function of the deformation β for $^{180-194}$Pb, $^{176-194}$Hg, $^{186-204}$Po, and $^{194-204}$Rn, respectively. The third 0^+ is displayed only when it presents a special interest. The $\bar{\beta}_{0k}$ value is indicated for each state by the symbols $\bullet(0_1^+)$, $\blacksquare(0_2^+)$, and $\blacktriangle(0_3^+)$, respectively.

For all Pb isotopes, the GCM ground state is predominantly spherical, in agreement with the data. The two lowest excited states are dominated by either oblate or prolate components. As we shall see below, the prolate state is lower in energy for the lighter isotopes up to $N = 106$ and the oblate one is lower above this value while they are nearly degenerate for $N = 106$. Although they are not separated by a sizable barrier, the spherical and oblate states are well separated. The occupation of intruder single-particle states in the oblate configuration seems to prevent a mixing. Indeed, at $\beta \simeq -0.15$, the downsloping $K = 7/2$ intruder orbital from the $2f_{7/2^-}$ shell above the spherical $Z = 82$ shell closure crosses the upsloping $3s_{1/2^+}$ orbital. In the same way, the prolate state does not mix significantly with the spherical and oblate states because its dominant contributions have a large occupation of several downsloping intruder levels on the prolate side.

The mean deformation $\bar{\beta}_{01}$ [Eq. (12)] for the ground states of ^{176}Hg and ^{178}Hg displayed in Fig. 9 is close to zero. Indeed, the small value of $\bar{\beta}_{01}$ is the result of a cancellation between the contributions of oblate and prolate configurations. This large mixing of different shapes can be related to flat energy curves

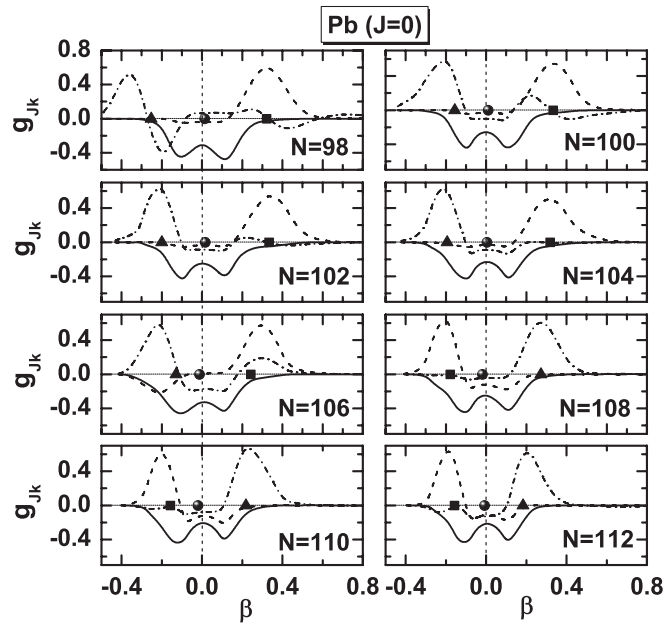

FIG. 8. Collective wave functions for the first two (solid and dashed curves) and some selected third (dash-dotted curves) 0^+ states in $^{180-194}$Pb. The mean deformations $\bar{\beta}_{Jk} \equiv \sum_q \beta(q)|g_{0k}(q)|^2$ are indicated with the symbols $\bullet(0_1^+)$, $\blacksquare(0_2^+)$, and $\blacktriangle(0_3^+)$.

given for these two isotopes in Fig. 3. For both isotopes, the first excited 0^+ state is prolate.

In fact, from the discussion of triaxial energy surfaces above, one can assume that both of these nuclei are soft in the γ degree of freedom that is not explicitly considered here. However, we recall that in symmetry restored GCM,

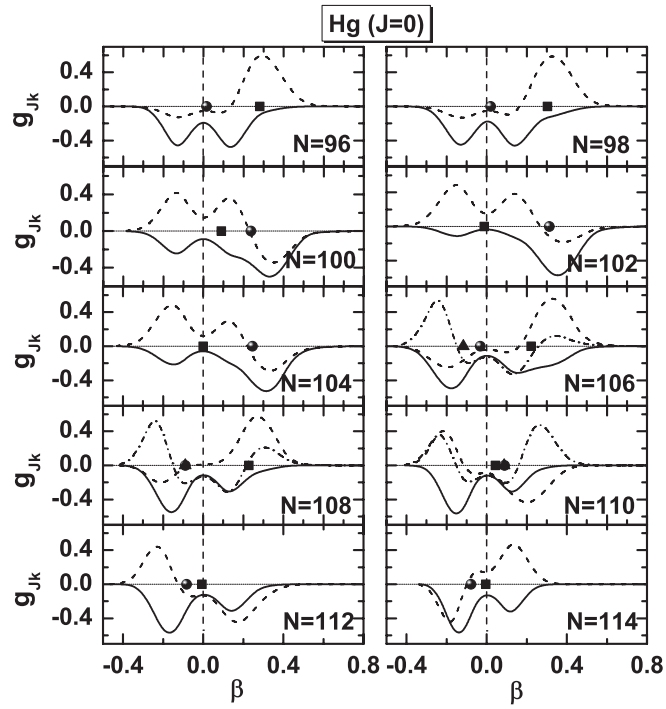

FIG. 9. Same as Fig. 8, but for $^{176-194}$Hg.

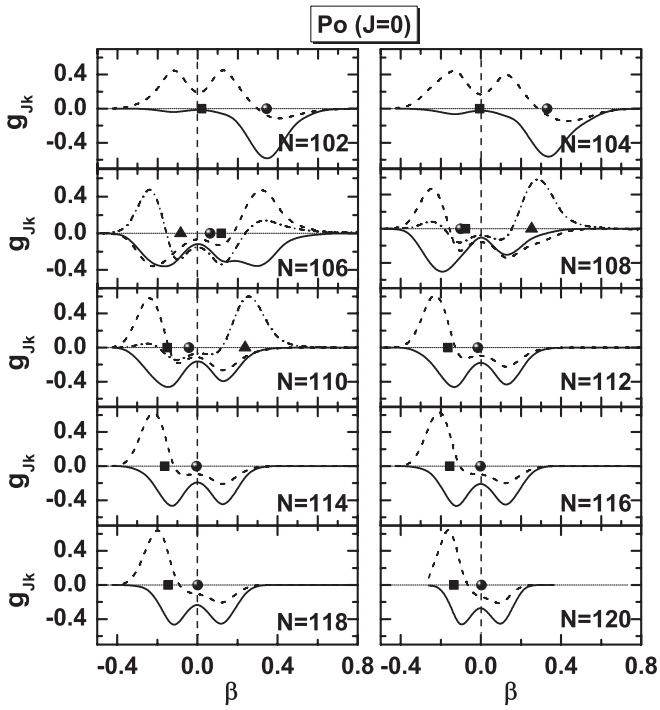

FIG. 10. Same as Fig. 8, but for $^{186-204}$Po.

prolate and oblate configurations are directly mixed by the Hill-Wheeler-Griffin equation, Eq. (3), independently of the height of a barrier on the axial path between them. Therefore, in an axial GCM calculation, as done here, one cannot distinguish the wave function of a γ-soft nucleus from that resulting from large mixing of two minima separated by a barrier.

For the Hg isotopes $100 \leqslant N \leqslant 104$, the prolate configuration is the ground state in contradiction with the data, as we shall see below, and the first excited 0^+ state is a spread state. The balance between oblate and prolate configurations in the ground state is reversed above $N = 104$, with a larger weight on the oblate side for the heaviest isotopes represented in the figure. The first excited 0^+ state is predominantly prolate for

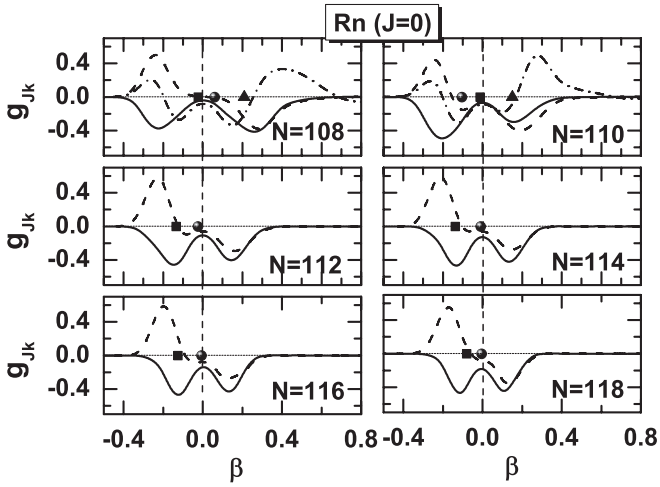

FIG. 11. Same as Fig. 8, but for $^{194-204}$Rn.

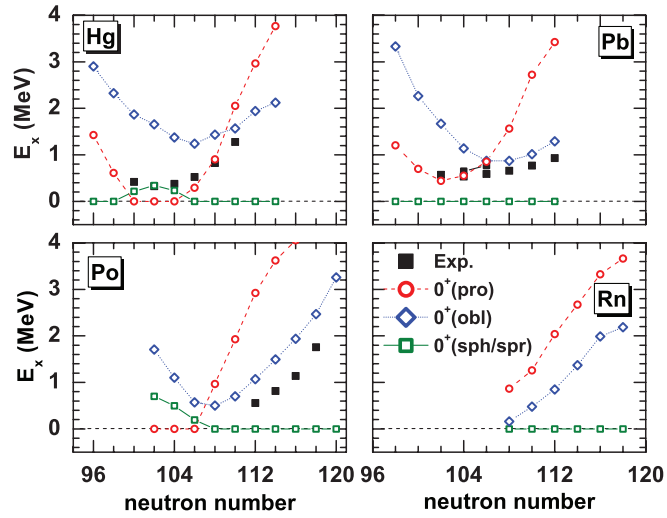

FIG. 12. (Color online) Systematics of excitation energy of first three 0^+ states in Hg, Pb, Po, and Rn isotopes. Lines connect the states with similar dominant configurations. The available experimental data [16,47,48] for the low-lying 0^+ states are plotted for comparison.

$N = 96$, 98, 106, and 108 and has a large spreading above 108. The second-excited state is oblate for $N = 106$ and 108.

For the Po isotopes, the ground states for $N = 102$ and 104 are the only ones to be dominated by prolate configurations. The ground states of the heavier isotopes have a large spreading. Figure 5 indicates that, for these isotopes, the almost equal mixing of prolate and oblate configurations results from the γ softness of their energy surface. The mean deformation $\bar{\beta}_{Jk}$ of excited states for $102 \leqslant N \leqslant 106$ is small, reflecting the nearly equal weight of oblate and prolate configurations. From $N = 108$ to the heaviest Po isotopes studied here, the first excited 0^+ state is dominated by oblate components, whereas the second excited one is prolate for $N = 108$ and 110. Experimentally, the ground states of the Po isotopes are interpreted as being spherical down to $N = 112$. The lighter isotopes are inferred to posses deformed ground states [5].

The collective wave functions of the Rn isotopes behave in a way similar to those of their Po isotones.

2. *Excitation energies*

The evolution of the energy of the first excited 0^+ states is compared to the experimental data in Fig. 12. The main findings are as follows:

(i) Going from $N = 120$ down to $N = 108$, the 0_2^+ and 0_3^+ excitation energies decrease rapidly in all the four isotopic chains, in agreement with the data.

(ii) As discussed above, the states 0_2^+ and 0_3^+ in Pb isotopes all have a well-defined shape, the 0_2^+ level being oblate above $N = 106$ and prolate below. The oblate and prolate configurations cross at $N = 106$; in this nucleus the excitation energies of the 0_2^+ and 0_3^+ states are quite close and below 1 MeV.

(iii) The evolution of the energy of the 0_2^+ state in Hg isotopes is in agreement with the data. In our calculations,

this state can be called prolate only for $N = 96$, 98, 106, and 108; for all other isotopes, it has a very spread character. Also, for $100 \leqslant N \leqslant 104$, the agreement between calculations and data is fortuitous, since our calculations do not reproduce the shape of the ground state deduced from the data.

(iv) For Po isotopes, the calculations overestimate the excitation energy of the 0_2^+ level but reproduce the slope of the variation of the energy with N. For all isotopes for which data exist, our calculations predict the 0_2^+ state to be oblate.

3. Variation of mean-square charge radii

The variation of the calculated mean-square charge radii is compared in Fig. 13 with the values deduced from the measured isotopic shifts. Our results for the Pb isotopes obtained with the SLy6 and SLy4 Skyrme parametrizations, each used with a different pairing strength, have already been compared with the data in Ref. [33]. In Ref. [18], results obtained with the SLy4 parametrization and two different values of the pairing interaction strength have been confronted with data. In both cases, it was observed that charge radii are extremely sensitive to the amount of mixing of mean-field wave functions corresponding to different shapes, which in turn is very sensitive to the pairing strength.

A sudden increase of the charge radii is obtained at $N = 104$ in our calculation for the Hg isotopes. It is related to the shape transition seen in Figs. 3 and 9 that is, however, not corroborated by the data. By contrast, a jump of similar size has been observed in odd-A Hg [11,13]. This observation indicates that two states based on either prolate or oblate shapes indeed coexist but that our calculations do not predict correctly their relative position. Above $N = 104$, the ground-state wave functions are weakly oblate, but become strongly peaked at prolate shapes for $100 \leqslant N \leqslant 104$, as shown in Fig. 9. However, this onset of large prolate deformation in the ground state is in contradiction with the experimental data. Clearly, the dominant configuration of the ground state should not change much down to at least $N = 102$.

The calculated charge radii overestimate the experimental ones below $N = 112$. The origin of this discrepancy has been discussed in Ref. [18] where we have shown that charge radii are very sensitive to the amount of mixing of different shapes in the collective wave function. A slight modification of this mixing could reduce the discrepancy between theory and experiment but it is unfortunately not possible to determine which component of the effective interaction has to be modified.

In the Rn isotopes, the kink at $N = 112$ in the calculated values of $\delta\langle r_{\rm ch}^2\rangle$ is due to the onset of weakly oblate deformations in the ground state at $N = 110$, cf. Figs. 9 and 12.

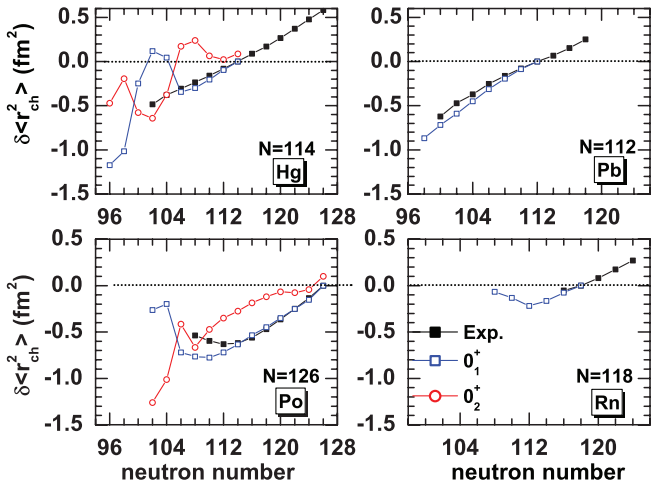

FIG. 13. (Color online) (Upper panel) Variation of the charge radii $\delta\langle r_{\rm ch}^2\rangle$ for the lowest 0^+ states in Hg [normalized to the ground state (g.s.) of ^{194}Hg], Pb (normalized to the g.s. of ^{194}Pb), Po (normalized to the g.s. of ^{210}Po), and Rn (normalized to the g.s. of ^{204}Rn) isotopes, compared to the the experimental data for ground states taken from Refs. [18,49].

4. Monopole transition strength

Figure 14 displays the $E0$ strength ρ_{E0}^2, Eq. (10), between the 0_2^+ and the 0_1^+ states. This electric monopole transition strength is correlated to the size of the deformation and to the amount of mixing between configurations corresponding to different shapes [2]. In general, large $E0$ strength arises from a strong mixing between states with different radii.

Compared to the very sparse experimental data that exist for some Hg, Pb, and Po isotopes, our calculated ρ_{E0}^2 values are too large by an order of magnitude. According to Ref. [2], this indicates an excessively strong mixing of configurations with different deformation in at least one of the two 0^+ states.

F. Low-lying states in $N = 106$ isotonic chain

After the discussion of the $J = 0$ states, we will now turn to the properties of states with finite angular momentum. Before looking at their systematics, let us first analyze how these

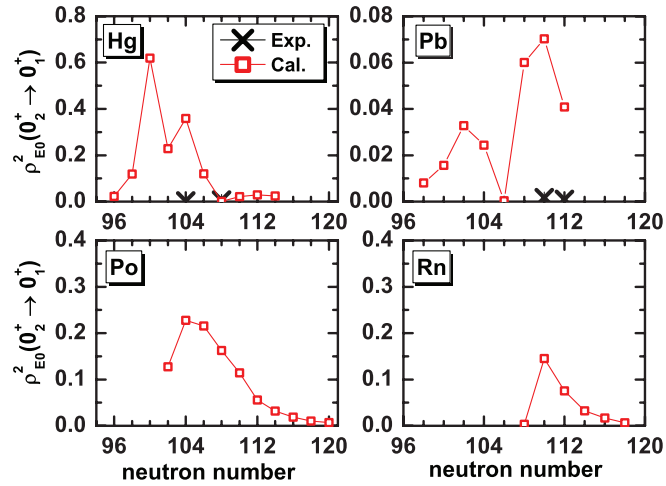

FIG. 14. (Color online) Electric monopole transition strengths ρ_{E0}^2 for the transitions between the first excited 0^+ state and the ground state (cf. Fig. 12) in Hg, Pb, Po, and Rn isotopes. Experimental data are taken from Ref. [50].

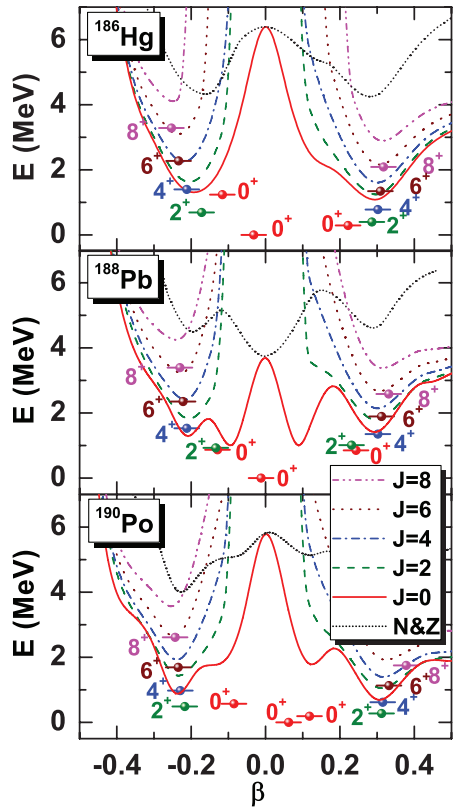

FIG. 15. (Color online) Deformation energy curves projected onto particle number (N&Z), or additional onto angular momentum ($J = 0, 2, \ldots, 8$), as well as the projected GCM states in the $N = 106$ ^{186}Hg, ^{188}Pb, and ^{190}Po isotones. The projected energy curves are plotted as a function of the intrinsic deformation β of the mean-field states. The energies of projected GCM states are indicated by bullets and horizontal bars placed at the average deformation $\bar{\beta}_{Jk}$. All energies are normalized to the 0^+ ground state.

levels group into bands in the case of the $N = 106$ isotones. For this neutron number, our calculations predict three nearly degenerate 0^+ levels for Hg, Pb, and Po, cf. Figs. 8-10, which makes these isotopes the ideal laboratory for this purpose.

The projected energy curves are plotted in Fig. 15 for ^{186}Hg, ^{188}Pb, and ^{190}Po. The energy of the correlated GCM states are indicated by bars located at their mean deformation $\bar{\beta}_{Jk}$. The energy curves projected only on particle numbers are also provided for comparison. There is no rotational band on top of the ground state of ^{188}Pb, which confirms our interpretation that this level is a correlated spherical state. However, the mean deformations $\bar{\beta}_{Jk}$ and energies of the GCM states, as well as the systematics of $B(E2)$ values and spectroscopic quadrupole moments to be discussed below, indicate two rotational bands in this nucleus, one of prolate and the other of oblate deformation. Similar bands are found for ^{186}Hg and ^{190}Po. For both bands and in all three isotones, the 0^+ band head is strongly perturbed.

The energy of the 0^+ band head is even pushed above that of the 2^+ state for the oblate band in Hg and Po and quasidegenerate in Pb. For larger-J values the bands, however, become more regular with a steady increase of the mean deformation $\bar{\beta}_{Jk}$ as a function of J. This means that deformation follows closely the minimum of the projected energy curve for the oblate bands, whereas it is becoming larger for the prolate sequences. In any event, a third low-lying 0^+ state that cannot be associated with a rotational band is also found for ^{186}Hg and ^{190}Po.

The theoretical spectra of the three nuclei are compared with the experimental data in Fig. 16. Note that the experimental data do not enable us to relate the two experimental excited 0^+ levels in ^{188}Pb to one of the two rotational bands that can be clearly visible at higher spins. As already discussed in previous studies [31], the calculated spectra are too expanded. However, the overall trends of experiment are rather nicely reproduced. The intraband $E2$ transition strength $B(E2 : J + 2 \rightarrow J)$ increases steadily with angular momentum, which is consistent with the picture shown in Fig. 15 that the collective wave functions are mainly built from either purely prolate or oblate mean-field states as soon as $J \geqslant 2$. Both

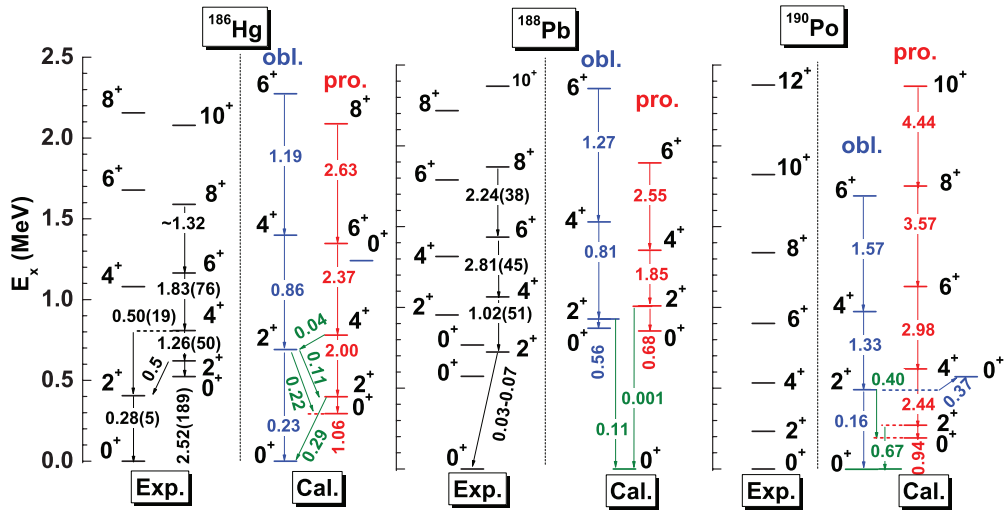

FIG. 16. (Color online) Comparison between the calculated and the measured low-lying spectra for ^{186}Hg, ^{188}Pb, and ^{190}Po. The $B(E2)$ values are given in e^2b^2 units. The experimental data are taken from Refs. [8,17,51–55].

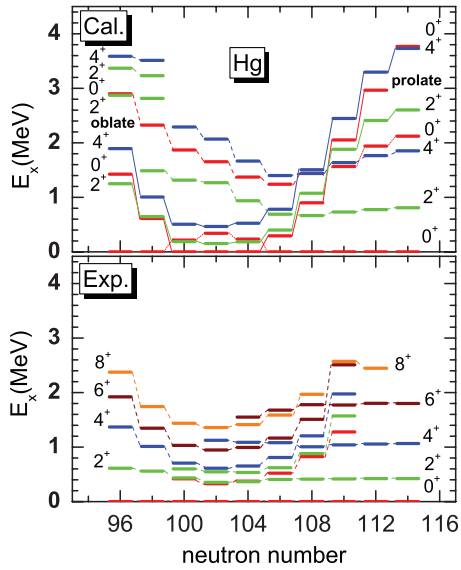

FIG. 17. (Color online) Systematics of calculated (upper panel) and experimental (lower panel) low-lying 0^+, 2^+, and 4^+ states in the Hg isotopes. The experimental data for the lowest 6^+ and 8^+ states are given as well to indicate the evolution of the band structure.

the experimental B(E2) values within and out of bands are reproduced satisfactorily by our calculation.

G. Systematics of 2^+ and 4^+ states

The variation as a function of N of the excitation energies of the low-lying 0^+, 2^+ and 4^+ states are presented in Figs. 17–20 for the Hg, Pb, Po, and Rn isotopes. The experimental data are taken from Refs. [16,47,48,56,57]. Lines join levels with a similar structure in two successive isotopes.

As already discussed for the $N = 106$ isotones, the spectra are expanded too much. There can be several sources to this deficiency: a variational space that is better suited to optimize

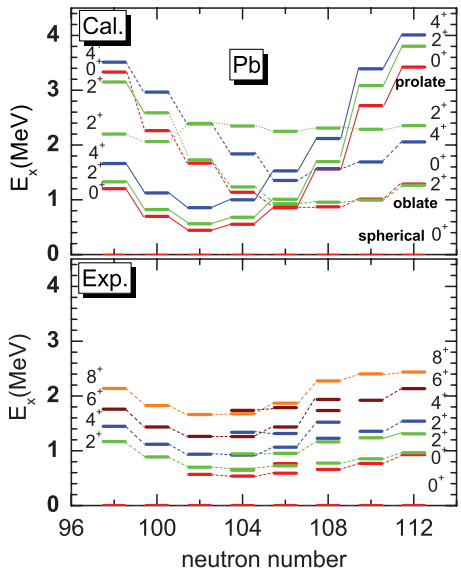

FIG. 18. (Color online) Same as Fig. 17, but for the Pb isotopes.

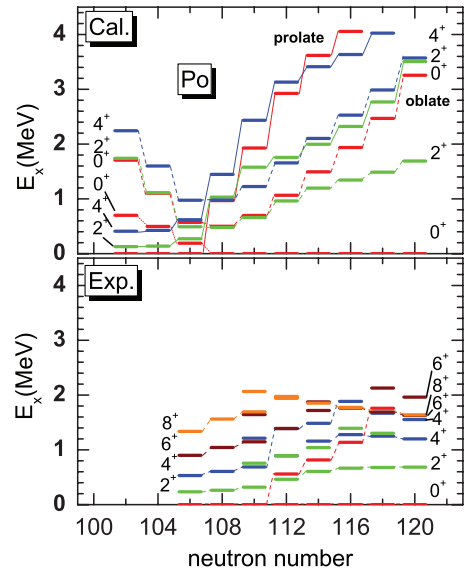

FIG. 19. (Color online) Same as Fig. 17, but for the Po isotopes.

the 0^+ ground state than the excited states, triaxiality effects, the treatment of pairing correlations, or deficiencies of the energy density functional. We will focus on the evolution of the relative position of the rotational bands as a function of N (and sometimes of Z), for which the spacing between levels in a band is in general not crucial. The main findings are as follows:

(i) The experimental trends are reasonably well reproduced by our calculations for the Hg and the Pb isotopic chains. In Pb, the prolate and the oblate bands cross between $N = 108$ and $N = 106$, in agreement with the data. For the Hg isotopes, there is an exchange of structure between the ground state and the first excited 0^+ level in such a way that we obtain a prolate ground state at $N = 104$ to 100, in contradiction with the data. However, the first two 0^+ states remain close in energy for these three isotopes.

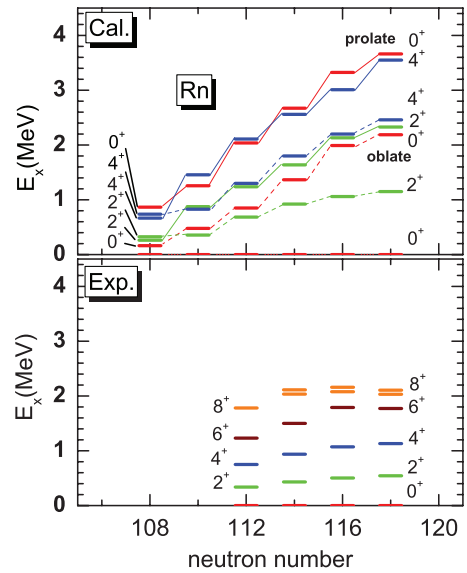

FIG. 20. (Color online) Same as Fig. 17, but for the Rn isotopes.

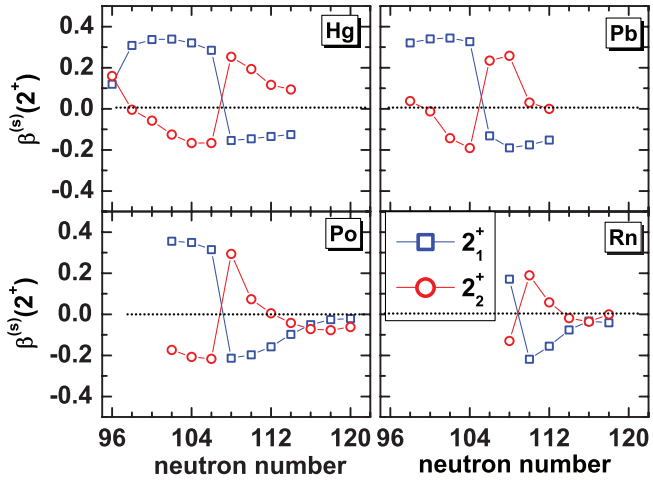

FIG. 21. (Color online) Quadrupole deformations $\beta^{(s)}$ [cf. Eq.(8)] of the two lowest $J = 2$ states calculated from the corresponding spectroscopic quadrupole moments as functions of the neutron number.

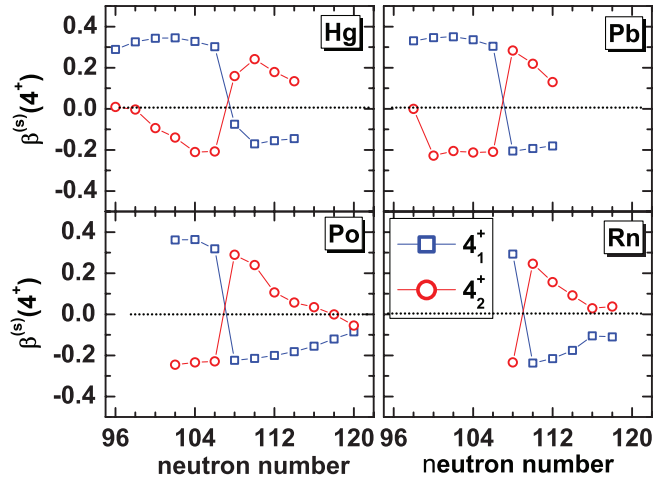

FIG. 22. (Color online) Same as Fig. 21, but for the $J = 4$ states.

(ii) In Hg and Pb, the mixing between the 0^+ levels is usually too large in the calculations, distorting too much the rotational character of bands at low spin. Experimentally, the energy of the first 2^+ level is nearly constant over the entire isotopic Hg chain, whereas its variation is much larger in our calculations. The energy difference between the 2^+ and 4^+ levels varies in a manner more similar to the data than the excitation energy of the 2^+ level.

(iii) In the Hg and Pb isotopic chains, the calculated excitation energies of the 2^+_1 and 4^+_1 levels reach their lowest value at $N = 102$. This result agrees with the experimental data for the Hg isotopes. For the Pb isotopes, the lowest excitation energy for these levels is obtained in the experimental data at $N = 104$, but the calculated results at $N = 102$ and 104 are only marginally different.

(iv) There is a clear disagreement between calculations and experimental data for the heavy Po isotopes. The overestimation of energies is close to a factor of two and much larger than for other nuclei. In particular, the near-constant value of the experimental 2^+ level energy between $N = 120$ and 112 is not reproduced at all. Being close to the $N = 126$ shell closure, these isotopes are probably not collective and would require to include np-mh excitations that are not generated by a constraint on deformation. The calculated spectra are more realistic for the isotopes with $106 \leqslant N \leqslant 116$.

(v) The disagreement with the data is not as strong for the Rn isotopes. In particular, the energy difference between the 2^+ and 4^+ levels is closer to the experimental value.

The quadrupole deformation parameters determined from the spectroscopic quadrupole moment, $\beta^{(s)}$ [cf. Eq.(8)], are plotted as a function of the neutron number in Figs. 21 and 22 for the lowest two 2^+ and 4^+ states, respectively. This parameter, which is directly related to an observable, permits a much less ambiguous assignment of a prolate or an oblate character to the levels than the mean deformation $\bar{\beta}_{Jk}$ of the wave functions. A crossing between oblate and prolate configurations takes place at $N = 106$ for the Hg, Pb, and Po isotopes, at $N = 108$ for Rn. Again, this result is not confirmed by the data for the Hg isotopes. For the heaviest Po, and Rn isotopes, $\beta^{(s)}$ is very small. This is a sign that the 2^+ and 4^+ are probably not based on a deformed state but would be better described by np-mh excitations of the kind already mentioned above. This could also be at the origin of the much-too-large excitation energies that we have obtained for these 2^+ and 4^+ states (see Figs. 19 and 20); our purely collective GCM basis not being well suited to describe these states.

The quadrupole deformations $\beta^{(t)}(2^+_k \to 0^+_{k'})$ [cf. Eq.(9)], corresponding to the electric quadrupole transition strengths $B(E2 : 2^+_k \to 0^+_{k'})$ are plotted in Fig. 23 for the transitions from the two first 2^+ to the 0^+ ground state and the 0^+_2 level, together

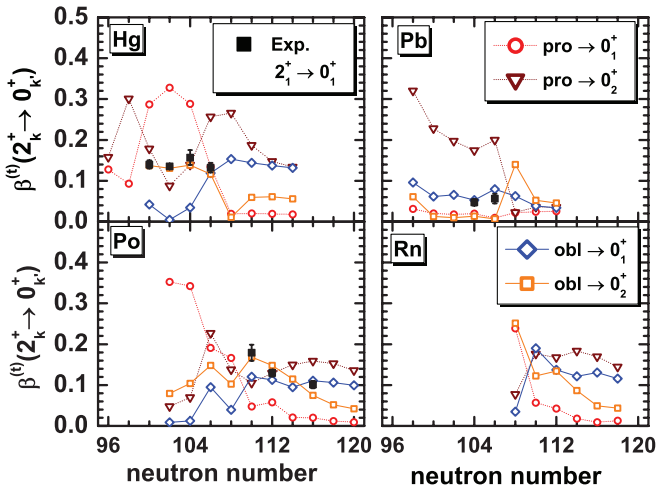

FIG. 23. (Color online) Systematics of the deformations $\beta^{(t)}$ derived from the reduced $E2$ strengths for the transition from the predominant prolate and oblate 2^+ states to the first two 0^+ states as a function of neutron number. The data for transition from the 2^+_1 state to the ground state are taken from Refs. [8,14,58–61].

with the available experimental data. The assignment of oblate and prolate labels to the 2^+ states are based on spectroscopic moments and are, thus, nonambiguous. The main findings are as follows:

(i) For ^{180,182,184}Hg, the experimental $\beta^{(t)}(2_1^+ \to 0_1^+)$ values are in good agreement with the calculated values for the transition from the oblate 2^+ level to the oblate 0_2^+ state. It shows also that theoretical transition probabilities can be accurate in spite of the fact that the energies and the order of levels are not reproduced.

(ii) For the Pb isotopes with $N = 104$ and 106, the experimental $\beta^{(t)}(2_1^+ \to 0_1^+)$ value is in good agreement with the calculated transition from the oblate 2^+ state to the spherical 0_1^+ state. It suggests that, with decreasing neutron number, the 2_1^+ state keeps predominantly an oblate character down to $N = 104$, beyond which the prolate 2^+ state becomes the yrast state in the calculations.

(iii) For the $N = 116$ Po isotope, the experimental $\beta^{(t)}(2_1^+ \to 0_1^+)$ value is reproduced quite well by the calculation. It corresponds to a transition from the oblate 2_1^+ level to the spherical 0_1^+ state. As the neutron number decreases to $N = 112$ and 110, the transitions calculated to the oblate 0_2^+ state are in better agreement with the experimental $\beta^{(t)}(2_1^+ \to 0_1^+)$ values than the transitions to the spherical 0_1^+ state. This indicates an onset of oblate deformation already at $N = 112$, which is consistent with the observation made from the experimental isotope shifts (cf. Fig. 13).

(iv) There are no experimental data for the $B(E2)$ values in the Rn isotopes discussed here.

H. Kinetic moment of inertia along yrast band

The variation of the moment of inertia along a band can be an indicator of its nature. There are well-established generic properties of the moments of inertia such as their increase with deformation, or that for the same value of $|\beta|$ the moment of inertia is larger for prolate deformations than for oblate ones. The kinetic moment of inertia $\Im^{(1)}$ is defined as

$$\Im^{(1)}(J) = \frac{\hbar\sqrt{J(J+1)}}{\omega(J \to J-2)}, \tag{13}$$

and the frequency ω,

$$\hbar\omega(J \to J-2) = \tfrac{1}{2}\,[E_x(J) - E_x(J-2)]. \tag{14}$$

The kinematic moments of inertia for transitions along the yrast line are plotted in Figs. 24–27 for transitions from $J = 2, 4, \ldots, 10$ to $J-2$ in Hg, Pb, Po, and Rn isotopes, respectively. As discussed above, the calculations underestimate the moment of inertia (cf. Fig. 16). To make the comparison with the experimental data easier, we have divided the calculated rotational frequency by a factor 1.50.

There are several common features in the four isotopic chains:

(i) For a static rotor, the kinematic moment of inertia is constant. The only nuclei in our sample which came close to this idealized case are the Hg isotopes with $N = 112$ and 114, at least up to $J = 8$ in both calculation and experiment. For all other nuclei the pattern is more complex.

(ii) The kinematic moment of inertia $\Im^{(1)}$ for $J = 2$ is significantly different from those corresponding to transitions from higher spins. This can be attributed to the ground-state configuration that in most cases is dominated neither by an oblate nor by a prolate configuration. In the Pb isotopes, the ground state is a correlated spherical state, with a very different structure from the first 2^+ state. In any case, the ground state cannot be considered as the band head of a rotational band.

(iii) The kinematic moments of inertia $\Im^{(1)}$ of states with spin $J \geqslant 4$ can be divided into two groups: the isotopes with $N \leqslant 106$ have a prolate configuration and a larger $\Im^{(1)}$, whereas the isotopes with $N > 108$ are oblate and have a smaller $\Im^{(1)}$. This feature is present in both the calculations and the data. This confirms again that

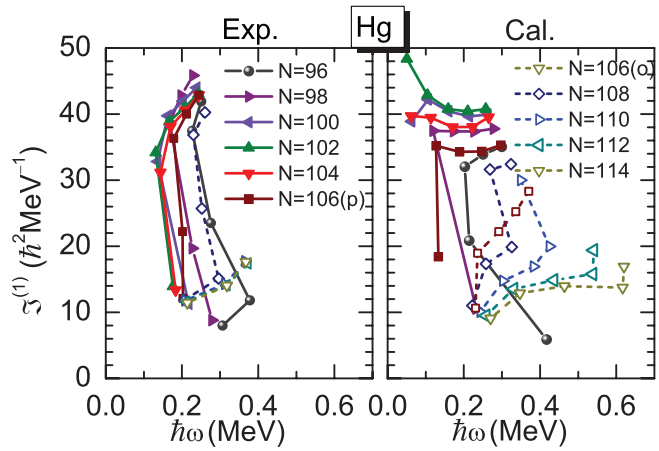

FIG. 24. (Color online) Kinematic moment of inertia $\Im^{(1)}(J)$ for Hg isotopes as a function of frequency $\omega(J \to J-2)$ for transitions along yrast line. For the calculated values on the right, $\hbar\omega$ has been scaled by a factor 1.50. Data on the left panel are taken from Ref. [47].

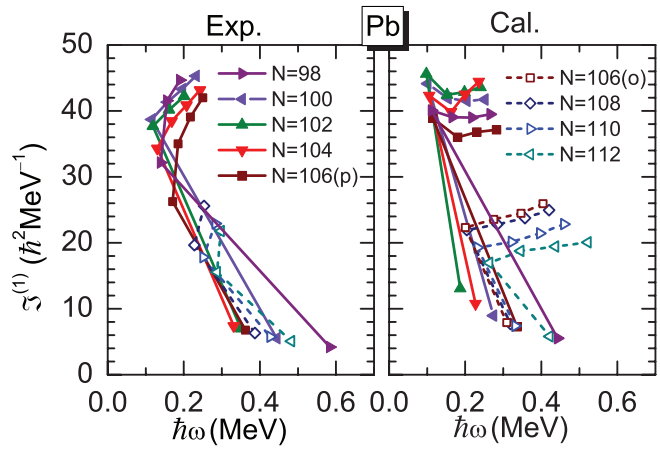

FIG. 25. (Color online) Same as Fig. 24, but for the Pb isotopes.

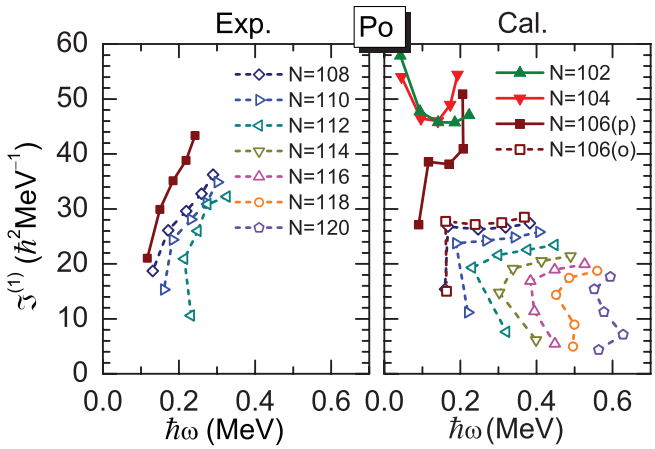

FIG. 26. (Color online) Same as Fig. 24, but for the Po isotopes.

prolate configurations dominate the yrast states below $N = 108$.

(iv) For many nuclei, the calculated $\Im^{(1)}$ moments take almost constant values for the highest angular momenta studied here. Such behavior, however, is almost never seen in the data. This discrepancy can be expected to have the same origins as the overall expansion of the spectra (cf. Sec. III G).

IV. SUMMARY AND OUTLOOK

We have shown that a detailed comparison between the results obtained by a beyond mean-field method and experimental spectroscopic data can be performed for a large number of nuclei. This comparison can be carried out without ambiguities when restoring quantum numbers and thereby selection rules for transitions. The region around the neutron-deficient Pb isotopes is of particular interest for such studies because it presents a very rich variety of phenomena, and the structure of these nuclei varies rapidly as a function of the neutron number.

The results of our model are in qualitative agreement with the experimental data. We obtain the coexistence of several

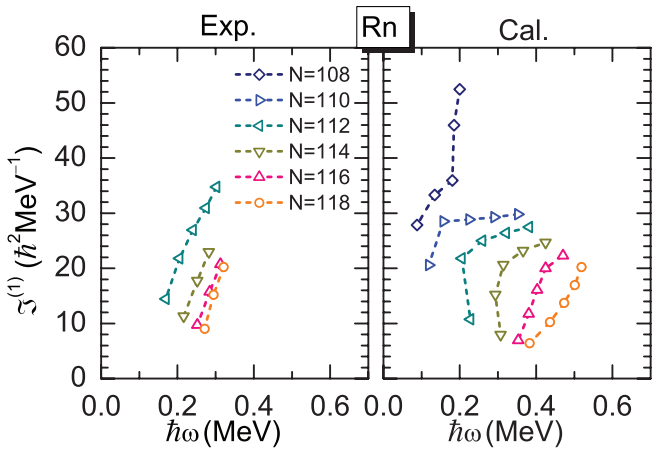

FIG. 27. (Color online) Same as Fig. 24, but for the Rn isotopes.

low-lying 0^+ levels showing mixing between oblate, prolate, and spherical configurations. The order of these levels is sometimes different from that deduced from the analysis of the data for α-decay hindrance, radii, moments of inertia, and electromagnetic transition densities. However, the theoretical $B(E2)$ values within a rotational band of given prolate or oblate nature are usually described well even though the relative position of the band heads is not correct.

We find that labeling states as oblate or prolate might not always be adequate, especially for nuclei in this mass region. In particular, the 0^+ and 2^+ states often result from a mixing between symmetry-restored mean-field wave functions corresponding to shapes spread over a wide range of deformations. The role of the mixing diminishes with increasing angular momentum, such that the spectra have more apparent rotational or vibrational character at high spin.

Our study has been limited to the mixing of particle-number and angular-momentum restored time-reversal invariant axial configurations. Tools to extend such calculations to triaxial shapes have been set up recently [26–28,62–64]. However, the presently available computational resources do not yet allow for their systematical application to very heavy nuclei. We have seen that triaxial configurations might play a role for some of the lightest Hg and some of the heaviest Po and Rn isotopes studied here. The absence of this degree of freedom is one of the reasons for the systematically too-expanded theoretical excitation spectra. To further improve the description of excited states, a second extension of the variational space to be considered in the future is the projection and mixing of time-reversal invariance-breaking mean-field states. On the one hand, starting from cranked Hartree-Fock-Bogoliubov (HFB) states that are optimized for finite angular momenta will incorporate the rotational alignment of single-particle states and the weakening of pairing correlations at high spin that comes with it. And on the other hand, the use of so-called blocked HFB states of the broken-pair type will provide a natural starting point to describe the noncollective states that can be suspected to dominate the low-lying excitation spectra of the heaviest Po and Rn isotopes discussed here. Developments in both directions are underway but, again, first applications will be limited to light nuclei for computational reasons.

The energy density functionals currently used do not permit us yet to reach an accurate quantitative description of spectroscopic data. However, we recall that the energy density functional used here has quite a simple form and that its parameters have been adjusted on the mean-field level to bulk properties of nuclear matter and magic nuclei. Hence, the overall good qualitative description of the rapidly evolving collective states of the nuclei studied here should be viewed as a success. This can be partially attributed to the generic features of the single-particle level schemes that remain an efficient tool to qualitatively analyze also results from beyond-mean-field calculations, as has been shown by our discussion. In addition to the well-known correlation between the opening and closing of gaps around the Fermi energy in the Nilsson diagram and the appearance of the various minima in the deformation energy surfaces, we have also seen that the spread of the correlated collective wave functions over different deformations is correlated with the deformations

at which the intruder levels cross the single-particle levels occupied in the spherical configuration. In general, we find that the mixing of states with a different number of occupied intruder levels is disfavored, which is consistent with the usual classification of shape coexisting states in the interacting shell model. A better quantitative description of fine details of shape coexistence, such as the relative energy between oblate and prolate band heads in the Hg isotopes below $N = 108$, will require improved single-particle energies; cf. also the discussion in Ref. [65]. First explorative studies in this direction indicate, however, that it is unlikely to obtain a significantly better description of single-particle energies by a refit within the current standard form of the energy density functionals [66,67], and that extensions are needed. Work in this direction is also underway.

ACKNOWLEDGMENTS

We thank R. Janssens and P. Van Duppen for useful comments on this manuscript. This research was supported in parts by the PAI-P6-23 of the Belgian Office for Scientific Policy, the National Science Foundation of China under Grants No. 11105111 and No. 10947013, the Fundamental Research Funds for the Central Universities (XDJK2010B007), the European Union's Seventh Framework Programme ENSAR under grant agreement n262010, by the French Agence Nationale de la Recherche under Grant No. ANR 2010 BLANC 0407 "NESQ", and by the CNRS/IN2P3 through the PICS No. 5994. A part of the computations was performed using HPC resources from GENCI-IDRIS (Grants No. 2007-050707, 2008-050707, and 2009-050707).

[1] K. Heyde, P. Van Isacker, M. Waroquier, J. L. Wood, and R. A. Meyer, Phys. Rep. **102**, 291 (1983).
[2] K. Heyde and R. A. Meyer, Phys. Rev. C **37**, 2170 (1988).
[3] J. L. Wood, K. Heyde, W. Nazarewicz, M. Huyse, and P. Van Duppen, Phys. Rep. **215**, 101 (1992).
[4] R. Julin, K. Helariutta, and M. Muikku, J. Phys. G **27**, R109 (2001).
[5] K. Heyde and J. L. Wood, Rev. Mod. Phys. **83**, 1467 (2011).
[6] P. Van Duppen and M. Huyse, Hyperfine Interact. **129**, 149 (2000).
[7] A. N. Andreyev *et al.*, Nature (London) **405**, 430 (2000).
[8] A. Dewald *et al.*, Phys. Rev. C **68**, 034314 (2003).
[9] K. Vyvey *et al.*, Phys. Rev. C **69**, 064318 (2004).
[10] M. Ionescu-Bujor *et al.*, Phys. Rev. C **81**, 024323 (2010).
[11] J. Bonn, G. Huber, H.-J. Kluge, L. Kugler, and E. W. Otten, Phys. Lett. B **38**, 308 (1972).
[12] J. Bonn, G. Huber, H.-J. Kluge, and E. W. Otten, Z. Phys. A **276**, 203 (1976).
[13] S. Raman, C. W. Nestor, Jr., and P. Tikkanen, At. Data Nucl. Data Tables **78**, 1 (2001).
[14] T. Grahn *et al.*, Phys. Rev. C **80**, 014324 (2009).
[15] I. G. Bearden *et al.*, Nucl. Phys. A **576**, 441 (1994).
[16] J. Elseviers *et al.*, Phys. Rev. C **84**, 034307 (2011).
[17] K. Van de Vel *et al.*, Phys. Rev. C **68**, 054311 (2003).
[18] T. E. Cocolios *et al.*, Phys. Rev. Lett. **106**, 052503 (2011).
[19] P. Van Duppen, E. Coenen, K. Deneffe, M. Huyse, K. Heyde, and P. Van Isacker, Phys. Rev. Lett. **52**, 1974 (1984).
[20] K. Heyde, J. Jolie, J. Moreau, J. Ryckebusch, M. Waroquier, P. Van Duppen, and M. Huyse, Nucl. Phys. A **466**, 189 (1986).
[21] V. Hellemans, R. Fossion, S. De. Baerdemacker, and K. Heyde, Phys. Rev. C **71**, 034308 (2005).
[22] V. Hellemans, S. De Baerdemacker, and K. Heyde, Phys. Rev. C **77**, 064324 (2008).
[23] J. L. Egido and L. M. Robledo, in *Extended Density Functionals in Nuclear Physics*, edited by G. A. Lalazissis, P. Ring, and D. Vretenar, Lecture Notes in Physics, Vol. 641 (Springer, Berlin, 2004), p. 269.
[24] M. Bender, Eur. Phys. J. Spec. Top. **156**, 217 (2008).
[25] T. Nikšić, D. Vretenar, and P. Ring, Phys. Rev. C **74**, 064309 (2006).
[26] M. Bender and P.-H. Heenen, Phys. Rev. C **78**, 024309 (2008).
[27] J. M. Yao, J. Meng, P. Ring, and D. Vretenar, Phys. Rev. C **81**, 044311 (2010).
[28] T. R. Rodríguez and J. L. Egido, Phys. Rev. C **81**, 064323 (2010).
[29] M. Bender, P.-H. Heenen, and P. Bonche, Phys. Rev. C **70**, 054304 (2004).
[30] T. Duguet, M. Bender, P. Bonche, and P.-H. Heenen, Phys. Lett. B **559**, 201 (2003).
[31] M. Bender, P. Bonche, T. Duguet, and P.-H. Heenen, Phys. Rev. C **69**, 064303 (2004).
[32] T. Grahn *et al.*, Nucl. Phys. A **801**, 83 (2008).
[33] H. De Witte *et al.*, Phys. Rev. Lett. **98**, 112502 (2007).
[34] P. Rahkila *et al.*, Phys. Rev. C **82**, 011303(R) (2010).
[35] D. L. Hill and J. A. Wheeler, Phys. Rev. **89**, 1102 (1953); J. J. Griffin and J. A. Wheeler, *ibid.* **108**, 311 (1957).
[36] D. Lacroix, T. Duguet, and M. Bender, Phys. Rev. C **79**, 044318 (2009).
[37] P. Ring and P. Schuck, *The Nuclear Many-Body Problem* (Springer, Heidelberg, 1980).
[38] M. Bender, P.-H. Heenen, and P.-G. Reinhard, Rev. Mod. Phys. **75**, 121 (2003).
[39] E. Chabanat, P. Bonche, P. Haensel, J. Meyer, and R. Schaeffer, Nucl. Phys. A **635**, 231 (1998); **643**, 441(E) (1998).
[40] C. Rigollet, P. Bonche, H. Flocard, and P.-H. Heenen, Phys. Rev. C **59**, 3120 (1999).
[41] See Supplemental Material at http://link.aps.org/supplemental/10.1103/PhysRevC.87.034322 for detailed spectroscopic results computed for total angular momentum values up to $J = 10\hbar$, in the neutron-deficient $^{176–194}$Hg, $^{180–194}$Pb, $^{186–210}$Po and $^{194–204}$Rn isotopes.
[42] R. R. Rodriguez-Guzman, J. L. Egido, and L. M. Robledo, Phys. Rev. C **69**, 054319 (2004).
[43] M. Bender, G. F. Bertsch, and P.-H. Heenen, Phys. Rev. C **73**, 034322 (2006).
[44] B. G. Carlsson, J. Toivanen, and A. Pastore, Phys. Rev. C **86**, 014307 (2012).
[45] Bruyeres-le-châtel database [http://www-phynu.cea.fr/science_en_ligne/carte_potentiels_microscopiques/noyaux/zz80/zz80n100all.html].
[46] P. Möller, R. Bengtsson, B. G. Carlsson, P. Olivius, and T. Ichikawa, Phys. Rev. Lett. **97**, 162502 (2006).
[47] National Nuclear Data Center, Brookhaven National Laboratory [http://www.nndc.bnl.gov/].
[48] R. D. Page *et al.*, Phys. Rev. C **84**, 034308 (2011).
[49] I. Angeli, At. Data Nucl. Data Tables **87**, 185 (2004).

[50] T. Kibédi and R. H. Spear, At. Data Nucl. Data Tables **89**, 77 (2005), and references therein.
[51] D. Proetel, R. M. Diamond, and F. S. Stephens, Phys. Lett. B **48**, 102 (1974).
[52] W. C. Ma *et al.*, Phys. Rev. C **47**, R5 (1993).
[53] P. Joshi *et al.*, Int. J. Mod. Phys. E **3**, 757 (1994).
[54] M. Scheck *et al.*, Phys. Rev. C **83**, 037303 (2011).
[55] http://ie.lbl.gov/TOI2003/GammaSearch.asp.
[56] G. D. Dracoulis *et al.*, Phys. Rev. C **69**, 054318 (2004).
[57] J. Pakarinen *et al.*, Phys. Rev. C **75**, 014302 (2007).
[58] N. Rud, D. Ward, H. R. Andrews, R. L. Graham, and J. S. Geiger, Phys. Rev. Lett. **31**, 1421 (1973).
[59] C. Ellegaard *et al.*, Nucl. Phys. A **206**, 83 (1973).
[60] T. Grahn *et al.*, Phys. Rev. Lett. **97**, 062501 (2006).
[61] N. Kesteloot, Master thesis, University of Leuven, 2010.
[62] J. M. Yao, H. Mei, H. Chen, J. Meng, P. Ring, and D. Vretenar, Phys. Rev. C **83**, 014308 (2011).
[63] T. R. Rodríguez and J. L. Egido, Phys. Lett. B **705**, 255 (2011).
[64] C. Bauer *et al.*, Phys. Rev. C **86**, 034310 (2012).
[65] M. Bender, P. Bonche, and P.-H. Heenen, Phys. Rev. C **74**, 024312 (2006).
[66] T. Lesinski, M. Bender, K. Bennaceur, T. Duguet, and J. Meyer, Phys. Rev. C **76**, 014312 (2007).
[67] M. Kortelainen, J. Dobaczewski, K. Mizuyama, and J. Toivanen, Phys. Rev. C **77**, 064307 (2008).